

X-ray Imaging with a Wedge-shaped Crystal Analyzer

Wanwisa Pattanasiriwisa^{a*}, Hiroshi Sugiyama^{b,c}, Anton Maksimenko^{b,c}, Masami Ando^{b,c} and Takehiko Ishii^a

^a National Synchrotron Research Center (NSRC), 111 University Avenue, Muang District, Nakhon Ratchasima 30000, Thailand.

^b Photon Factory, Institute of Material Structure Science, KEK, 1-1 Oho, Tsukuba, Ibaraki 305-0801, Japan.

^c Department of Photo-Science, School of Advanced Studies, Graduate University for Advanced Studies, 1-1 Oho, Tsukuba, Ibaraki 305-0801, Japan.

* Corresponding author, E-mail: wanwisa@nsrc.or.th

Received 27 Dec 2004

Accepted 8 Nov 2006

ABSTRACT: The advantage of X-ray imaging by the use of synchrotron radiation and a wedge-shaped crystal analyzer is shown. The experiments have been carried out using synchrotron radiation from a 5T superconducting wiggler in a 2.5 GeV storage ring. Striped image patterns characteristic of a wedge-shaped crystal analyzer are clearly observed. Results on breast cancer phantoms and an ant show images with good contrasts revealing the interiors of the samples in case of dark field images, which are not seen in bright field images. The physical process of the generation of a dark field image is simply explained. The obtained results present the experimental evidence for the basic assumption made in the explanation of the dark field imaging.

KEYWORDS: X-ray imaging, Breast phantom, Synchrotron radiation, X-ray dynamical diffraction, Medical Application.

INTRODUCTION

X-rays have a strong power to penetrate materials and this property is used to see the interior of a material. X-rays are scattered by atoms and this causes the diffraction of X-rays by a crystal. This nature of the interaction of x-rays with a crystal is utilized very usefully to identify the atomic arrangement of a crystal.

Simplest and most useful applications of X-rays are found in medical diagnoses. In medical diagnoses, X-rays that have passed through a body make a visual image of its interior structure when they strike a photographic film or a fluorescent screen. The darkness of shadows produced on the film or the fluorescent screen depends on the relative opacity of different parts of the body. The images obtained in this way tell us what are inside our bodies.

In recent years, synchrotron radiation in the X-ray region is used for scientific researches. The X-ray imaging application to coronary angiography^{1,2} is a representative example. Another expected example, which has been investigated up to the present, is X-ray dark field imaging. The *dark field image* (DFI) is formed by weak X-rays and has a good contrast of an image by removing the bright X-ray background.

The direction of the propagation of an X-ray in a material is slightly changed by scattering. This makes the penetrating X-ray beam more divergent than the X-

ray beam incident on a sample. This property is used to produce two kinds of X-ray beams with a crystal analyzer. Two kinds of *absorption* images of a sample can be made using two different x-ray beams. The phase of the X-ray wave is not considered here. The progress of the research can be found in refs. 3 – 10.

If the X-ray beam penetrating a sample straight falls on a crystal analyzer at a specific glancing angle, it is reflected by the Bragg reflection. This beam is referred to as the *reflected* beam. The intensity of the reflected beam is high. The beam consisting of X-rays in the slightly divergent portion does not satisfy the Bragg condition and proceeds straight in the crystal analyzer. This beam is referred to as the *direct* beam. X-rays penetrating out of a sample have the information of the two dimensional spatial distribution of the absorption coefficient. This beam makes the absorption image. The absorption image formed by the reflected beam is referred to as the *bright field image* (BFI). It is shown that the direct X-ray beam penetrating a crystal analyzer straight has a weak intensity and forms DFI.

If a wedge-shaped crystal blade is used for an analyzer, both DFI and BFI can be recorded on the same detector film. This facilitates the comparison of DFI and BFI and the efficiency of an experiment is increased considerably. At the same time, the basic assumptions made in the explanation of the formation of DFI are experimentally proved, since the conditions

for recording DFI and BFI are the same.

This report aims at presenting the physical aspects of the DFI generation using a simple model. In order to show the validity of the model, measurements of absorption images of an ant and breast cancer phantoms were carried out using a parallel plate crystal analyzer and a wedge-shaped crystal analyzer, respectively. Synchrotron radiation is used in both cases. The results of the measurements and discussion about the results are presented.

FORMATION OF DARK FIELD IMAGES

The DFI formation is described on the basis of a simple experimental arrangement as follows (Fig. 3). In this system, parallel monochromatic X-rays fall on a sample. X-rays having penetrated the sample are then incident on a crystal analyzer. The crystal analyzer separates the X-ray beam into the reflected and direct beams. Even if a perfectly parallel beam is incident on a sample, the beam coming out of the sample is slightly divergent owing to atomic scattering. Later, it will be shown that the use of a slightly divergent X-ray beam is important in the generation of separate DFI and BFI. The Bragg condition is written as

$$\lambda = 2d \sin \theta_b \quad (1)$$

Here, d is the distance between atomic net planes, λ is the wavelength and θ_b is the glancing angle of incidence. Only the condition of the first order reflection is given in (1). It is assumed that the center of the slightly divergent X-ray beam penetrating through a sample is incident on the crystal analyzer with an incident glancing angle of θ_b .

In the present study, the (440) plane of Si is used as the net plane of X-ray reflection by the crystal analyzer. The distance between the net planes is 5.43 \AA^{11} . If this value is inserted into (1), the Bragg angle for X-rays of 35 keV (0.354 \AA) used in the experiments is

$$\theta_b = 1.87^\circ \quad (2)$$

In the same way, the Bragg angle for X-rays of 1.54 \AA appearing in a reference is

$$\theta_b = 8.15^\circ \quad (3)$$

The X-ray beam propagating toward the direction that deviates from θ_b by an angle more than a critical value does not make the Bragg reflection.

The divergent part of the X-ray beam outside the critical reflection angle propagates straight in the crystal analyzer and forms the direct beam. The beam divergence of X-rays of 35 keV coming out of a 5 T

wiggler in a 2.5 GeV storage ring is about $61 \mu \text{ rad}^{12}$. Although this value is quite small, it is an order of magnitude larger than the width of the rocking curve of an almost perfect Si crystal for high index Bragg reflection. It is $0.5 \text{ arc. sec}^{13}$, which is $2.4 \mu \text{ rad}$. The half width is $1.2 \mu \text{ rad}$. In the optical system used, X-rays are monochromatized with three crystals before the beam falls on a sample. This beam is very parallel. The divergence is almost equal to that of the rocking curve. As mentioned before, this parallel beam is made divergent slightly by the sample. The crystal analyzer takes the central part of this divergent beam out and reflects it by the Bragg reflection. The width of the reflected beam is the same as that of the rocking curve of the crystal analyzer.

We consider an ideal case in which the crystal analyzer does not absorb x-rays. The crystal analyzer is installed in the way that the Laue geometry holds for the incident beam. Transmittance of the crystal analyzer is referred to as $T(\alpha)$ and the reflectance as $R(\alpha)$, where α is the renormalized angle of deviation from the Bragg angle.

The renormalized angle of deviation, α , is defined as

$$\alpha = a(\theta - \theta_b) \sin 2\theta + b \quad (4)$$

Here, θ is the glancing angle of incidence of the X-ray beam. Parameters a and b are complicated quantities derived through the dynamical theory of X-ray diffraction in a crystal. They include several complicated factors and terms. In this sense, α is a renormalized quantity. These renormalized quantities appear in the formalism describing the electromagnetic field in the crystal. It is not necessary to describe them explicitly here.

In a rigorous calculation, the transmittance and the reflectance are given as¹⁴

$$T = \sin^2(\pi\tau\sqrt{1+\psi^2}/\Lambda)/(1+\psi^2) \quad (5)$$

$$R = [\psi^2 + \cos^2(\pi\tau\sqrt{1+\psi^2}/\Lambda)]/(1+\psi^2) \quad (6)$$

$$T + R = 1 \quad (7)$$

$$\Lambda = \lambda \cos \theta_b / |P\chi_G| \quad (8)$$

where τ is the thickness of the crystal analyzer and ψ is a relative quantity defined as

$$\psi = \alpha / \alpha_c \quad (9)$$

Here, α_c is the value of α corresponding to that of the edge of the rocking curve. In (5) and (6), variable

ψ is used instead of α . The Bragg reflection occurs for α satisfying

$$|\alpha| \leq \alpha_c \tag{10}$$

This is equivalent to the condition

$$|\psi| \leq 1 \tag{11}$$

Λ is the extinction distance defined by (8). λ is the X-ray wavelength, P the polarization factor and χ_G the susceptibility. P is either 1 or $\cos 2\theta_B$ for each state of polarization. The susceptibility for X-rays with energies above 10 keV is very small. Since the value of χ_G of Si is not known for X-rays of 35 keV at present, we assume the magnitude to be 2×10^{-6} so that the good agreement of the calculated results with the observed results is obtained. The relation (7) holds for any values of ψ . Equations (5) through (8) are derived by solving the Maxwell equations in a crystal along with the diffraction conditions. Here it is emphasized that T and R given by (5) and (6), respectively, depend not only on ψ but also on τ . This gives rise to the X-ray penetration properties of a wedge-shaped crystal analyzer as will be mentioned later. With the postulated value of χ_G mentioned above and for a summit angle of 0.3° of the wedge, the thickness change of only $9 \mu\text{m}$ in the crystal analyzer changes the reflectance from the maximum to the minimum. This means that the crystal analyzer must be fabricated with an accuracy of $0.5 \mu\text{m}$. The thickness should not fluctuate much more than this value. It is somewhat difficult to fabricate a crystal blade to a given thickness with this accuracy. In this respect, it is more convenient to adjust λ instead of τ so that the Bragg condition is satisfied. The use of synchrotron radiation is essential in this respect, since we can select and adjust any required wavelength λ easily. One of characteristic properties of synchrotron radiation is used: It has a continuous spectrum with strong intensity.

Figure 1 shows the deviation angle dependence of the transmittance and the reflectance calculated with (5) and (6), respectively, for a small deviation angle region. The full line in the upper panel indicates the reflectance and that in the lower panel indicates the transmittance. The deviation angle, δ , is defined as the angle of difference between the direction of the incident beam and that of the center of the incident beam for which the highest Bragg reflection takes place. The deviation angle is equal to

$$\delta = \theta - \theta_B \tag{12}$$

δ appears already in (4). The reflectance curve represents the rate of reflection by crystal net planes (440). In the figure, the deviation angle given in the

abscissa is not ψ defined in (9) but the real one as given by (12). The magnitude of the abscissa is scaled by a factor of 2. This scaling leads to a better agreement of the width of the central band of the reflectance curve in Fig. 1 with the width of the rocking curve calculated in a different way¹⁵. This scaling does not affect the result on the separation of DFI from BFI presented in the present study.

The width of the rocking curve for the θ_B Bragg reflection of X-rays with a wavelength of 1.54 \AA from Si (440) planes is calculated to be 2.78 arc.sec . This value is equivalent to $13.0 \mu\text{rad}$. The width of the rocking curve, ω_s , is written as

$$\omega_s = C\lambda^2 / \sin 2\theta_B \tag{13}$$

where C is a constant. Using (13), we can evaluate the width of the rocking curve of the Si (440) reflection for X-rays with a wavelength of 0.354 \AA as

$$\begin{aligned} \omega_s &= 13.0 \times (0.354 / 1.54)^2 \times (\sin 16.3^\circ / \sin 3.74^\circ) \\ &= 2.96 (\mu\text{rad}) \end{aligned} \tag{14}$$

The width of the central band of the reflectance curve in Fig 1 is estimated at $3.2 \mu\text{rad}$.

Therefore, a fair agreement is obtained.

As seen in (5) and (6), the arguments of the trigonometric functions include the X-ray wavelength, λ , which is 0.354 \AA in the present case. With the value of χ_G being 2×10^{-6} , argument A of the trigonometric functions in (5) and (6) takes the value of

$$A(\psi) = 62.2\pi\sqrt{1 + \psi^2} \tag{15}$$

for the thickness of the analyzer crystal, τ , of 1.1 mm used in the present study. This point will be treated later again. Since $A(\psi)$ is large, T and R oscillate with small intervals of the deviation angle.

Two monochromators are installed in the beam line. Then, the X-ray beam incident on the sample is monochromatic and almost parallel. The angular divergence of this beam is almost that of the rocking curve with a divergence of $3.0 \mu\text{rad}$. The divergence angle of the X-ray beam coming out of the sample is characteristic of the sample and very small. We assume that the beam profile of X-rays incident on the crystal analyzer is as shown by the broken curve in Fig. 1.

Figure 1 also shows the angular divergence profile of the X-ray beam reflected by the net planes of the crystal analyzer satisfying the Bragg condition (reflected beam) and that of the X-ray beam penetrating the crystal analyzer without satisfying the Bragg condition (direct beam). The divergence of the reflected beam is shown in the upper panel and that of the direct beam in the

lower panel. The beam profile spectra are shown by dotted curves with hatches under them.

The X-ray beams are split by the Bragg reflection. In Fig. 1, the deviation angle dependence of the split beams is illustrated as curves RI_o (upper panel) and TI_o (lower panel), where I_o represents the intensity of the incident beams. In the figure, the I_o curves are depicted with broken lines. Magnitudes given in the ordinate are shown in the relative scale. The data of the profiles of the split beams shown in Fig. 1 is somewhat qualitative since the spectrum of the incident beam is qualitative. However, the results shown in Fig. 1 well indicate the separation of the direct and reflected beams.

The intensity of the direct beam, TI_o , is weak. It is 17% as intense as the reflected beam. The *absorption image* of the sample formed by the RI_o beam is BFI and

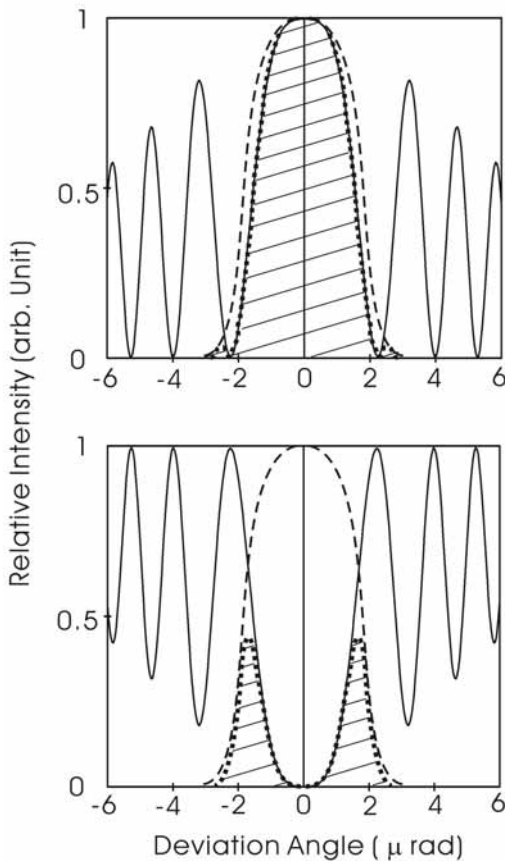


Fig 1. Profiles of the deviation angle dependence of reflected X-rays (upper panel) and that of penetrating X-rays (lower panel) for X-ray energy of 35 keV. The crystal is 1.1 mm thick. Broken lines: Profiles of X-rays, I_o , incident on the crystal analyzer. Full lines: Reflectance R (upper panel) and transmittance T (lower panel). Dotted lines with hatched areas: Profiles of reflected X-rays, RI_o , (upper panel) and penetrating X-rays, TI_o , (lower panel). The net reflection planes of analyzer crystal are Si (440). For the deviation angle, see text.

that formed by the TI_o beam is DFI. In case of BFI, the strong beam intensity causes the unnecessary background and the image contrast is reduced. On the other hand, the weak intensity of the TI_o beam does not cause the appreciable background and the good image contrast is obtained.

The propagation direction of the central portion of the beam is deflected from that of the incident beam by the crystal analyzer through the Bragg reflection. The deflected beam forms the reflected beam defined here. The Si (440) planes used in the present experiments deflect the beam by an amount of

$$2\theta_b = 3.74^\circ$$

If a detector film is placed at the point 50 cm apart from the crystal analyzer, the image by the reflected beam is obtained at the location 33 mm away from that by the direct beam. Since the width of the beam incident on the crystal analyzer and thus on the detector film is 16 mm in the present experiments, the reflected and direct beams are completely separated at the recorder position. Thus either BFI or DFI can be obtained on the detector film. If a 40 mm wide film was placed at the location 30 cm away from the crystal analyzer, both BFI and DFI on the same film would be recorded.

If the crystal analyzer is wedge-shaped, the situation is different. The analytical treatment of the X-ray beam in the wedge-shaped crystal analyzer based on the kinematical and dynamical theory is quite complicated and it is not practical to summarize the theoretical treatment here. In case of a wedge-shaped crystal analyzer blade, however, the image formation can be explained using (5) and (6). Equations (5) and (6) show that the transmittance and reflectance are dependent on the thickness, τ , of the crystal analyzer. Because of the large factor, $1/\Lambda$, a continuous, small change in τ gives rise to a fast, oscillatory variation in T and R . As will be explained in Fig. 2, the oscillatory intensity variation of the transmittance and the reflectance as a function of the blade thickness is transferred to the intensities to be recorded by a detector film. Thus, a wedge-shaped crystal analyzer is used, both BFI and DFI are formed on the same detector film alternately along a direction parallel to the wedge.

The observed results show that the image of the beam recorded on photographic film forms a white and dark stripe band pattern. From (5), (6) and (8), argument A of the trigonometric functions representing transmittance T and reflectance R of the crystal analyzer is written as

$$A(\psi, \tau) = \pi \tau |P\chi_G| \sqrt{(1 + \psi^2)} / \lambda \cos \theta_b \tag{16}$$

Since the Bragg angle is 1.87° , $\cos \theta_b$ is very near to

unity. The polarization factor, P , can be taken to be 1. The susceptibility is assumed to be $\chi_G = 2 \times 10^{-6}$. Thus, for X-rays with an energy of 35 keV which is equivalent to a wavelength of 0.354 \AA , we have

$$A(\psi, \tau) = \pi \tau \sqrt{1 + \psi^2} \times 5.65 \times 10^{-5} \quad (17)$$

Here, τ is given in nanometer units.

The discussion given below is not affected even if we put $\psi = 0$. Then we have

$$A(\tau) = \pi \tau \times 5.65 \times 10^{-5} \quad (18)$$

Suppose A changes by $\pi/2$ when τ changes by $\Delta\tau$. Then (18) becomes

$$\Delta\tau = 8.85 \text{ (\mu m)} \quad (19)$$

If the thickness of the crystal analyzer changes by this amount, the magnitudes of both transmittance T and reflectance R change their values from the maxima to the minima.

When we use a wedge-shaped analyzer, the striped bands occur on the film along the direction parallel to the wedge axis of the crystal analyzer. If the summit angle of the wedge is 0.34° , bands of dark and white stripes appear at every 3 mm position on the detector film. The generation of the two beams proceeding toward different directions in a wedge-shaped crystal is also explained by Batterman¹⁶.

Equation (7) indicates that the sum of the intensities of the reflected and direct beams equals to the intensity of the incident beam in the case where absorption by the crystal analyzer is neglected. If the intensity of the reflected beam is low owing to the effect of the thickness of the crystal analyzer, the intensity of the direct beam is high. Therefore, the dark and white stripe pattern is observed both in the reflected and direct beams.

Weak X-rays reach at the portion of the dark bands on the detector film. This is caused by the finite resolution and the situation that both ψ and τ determine the intensity variation. In this way, both BFI and DFI are recorded on the same film if a wedge-shaped crystal analyzer is used. The separation of the white and dark stripes was experimentally found to be 1.5 mm. The stripe pattern is practically enlarged in photographic printing and then inspected. The situation described above is shown in Fig. 2.

Figure 2, middle panel, shows how a crystal analyzer blade splits the incident X-ray beam into the reflected and direct X-ray beams. In the top panel of the figure shows the variation of the intensities of X-rays as thickness t of the crystal analyzer changes. The full line indicates the intensity of the reflected beam. The broken line exhibits the intensity of the direct beam. In

the bottom panel, the intensity variation on the detector film is depicted for either the reflected or direct beam. The coordinate in the direction parallel to the crystal analyzer is designated as x . The areas where DFI and BFI are expected to occur are designated as D and B, respectively.

The consideration made above appears to indicate that X-ray beams whose intensities vary in a sinusoidal manner fall on the detector film. In practice, the sensitivity of the film is saturated for a high intensity beam. Therefore the absorbance of the developed negative film is not proportional to the intensity of the X-ray beam in the high intensity region. Accordingly, it is assumed that the dark image area occurs for the intensity lower than 20 % of the maximum intensity. Apparently, the boarder between the BFI and the DFI regions can be defined clearly because of the sinusoidal variation of the intensity.

So far, the effect of the resolving power of the crystal analyzer have been ignored. In the case where the crystal net planes are parallel to the surface, the resolving power is independent of wavelength. For the

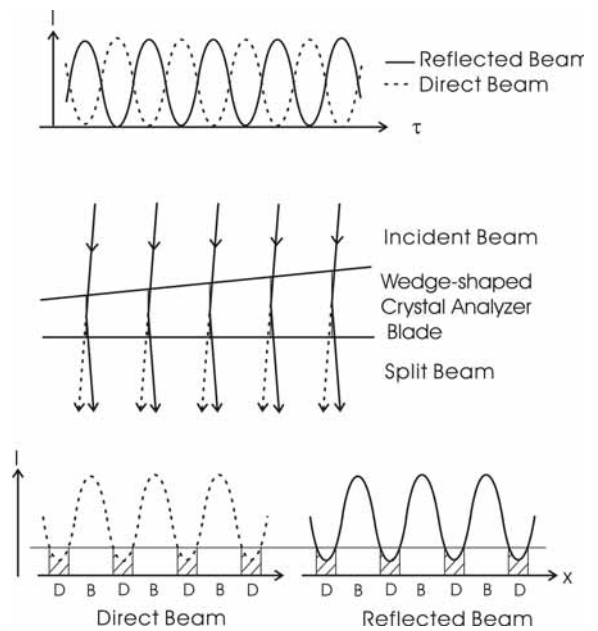


Fig 2. Variation of the X-ray intensity after the X-ray beam passes through a wedge-shaped crystal analyzer. Top panel: Intensity variation as the thickness of the crystal analyzer, τ , changes. The Bragg reflection occurs around particular values of τ . Full line indicates the intensity of the reflected beam. Broken line exhibits the intensity versus the thickness for the direct beam. Middle panel: Beam directions through a wedge-shaped crystal analyzer blade. Bottom panel: Intensity variation along the film. The site on the film is indicated as x . Areas where DFI and BFI are formed are indicated as D and B, respectively.

Si (440) plane, the resolving power is estimated to be¹⁵

$$\Delta\lambda / \lambda = 0.96 \times 10^{-5} \quad (20)$$

According to (1), the obscurity, $\Delta\theta$, of the reflection angle caused by $\Delta\lambda$ is given as

$$\Delta\theta = (\Delta\lambda / \lambda) \tan \theta_b \quad (21)$$

If we insert (20), the values of the Bragg angle, 1.87° , and wavelength, 0.354 \AA into (21), we obtain

$$\Delta\theta = 0.313 \text{ (}\mu\text{rad.)}$$

This changes the width of the rocking curve, ω_s , in (14) to

$$\omega_s = 0.298 \text{ (}\mu\text{rad.)}$$

Thus, the width of the rocking curve is not affected by the intrinsic obscurity in wavelength due to the resolving power.

The pioneering system of Ingal and Beliaevskaya⁷, Chapman *et al.*¹⁰ and Thomlinson *et al.*¹⁷ have shown that, in principle, near-dark-field imaging can be achieved by adjusting the reflection angle of the crystal analyzer. Therefore, one may need more than one exposure for collecting all dark field images in their methods.

EXPERIMENTAL METHODS

Experiments were carried out at the beam line, BL14B, of the Photon Factory of the High Energy Accelerator Research Organization (KEK). The conceptual illustration of the experimental arrangement is shown in Fig. 3. In the top panel, (a), the X-ray source and other optical elements are illustrated schematically. The X-ray source is a vertical wiggler. The wiggler works as a wavelength shifter. White synchrotron radiation X-rays from the wiggler is monochromatized with a double crystal monochromator. Then the narrow monochromatic X-rays are reflected with a collimator crystal. The collimator crystal further monochromatizes the X-rays from the monochromator. At the same time, the width of the beam is expanded. The crystal net planes are so aligned as to reflect the beam in this manner. The X-ray beam is also more collimated. Thus, nearly plane wave X-rays are sent to a sample and then to the crystal analyzer. Finally, the beam reaches a detector film to obtain the images of the sample.

In the middle panel, (b), the layout of two crystals for monochromatization is shown. By the Bragg reflection on the first mirror, monochromatic X-rays

are taken out. By the Bragg reflection by the second crystal, the monochromatized beam is reflected parallel to the incident white X-ray beam.

In the bottom panel, (c), the relation of the X-ray beams with a sample, a wedge-shaped crystal analyzer and a detector (X-ray film) are illustrated. The crystal deflecting X-rays from the monochromator and sending them to the sample was aligned for using asymmetric reflection to expand the beam size and to narrow the beam divergence at the experimental station. The wedged crystal analyzer manufactured on site was installed. Experiments were carried out under the following conditions: The average crystal thickness was 1.08 mm, the X-ray photon energy 35 keV, and the asymmetric parameter is 0.05. The current in the storage ring was approximately 400 mA.

In order to demonstrate the occurrence of striped imaging of BFI and DFI, we used mammographic phantom specimens were used. The spatial resolution of the observation system is determined by the beam width at the exit of the Bormann fan which is formed

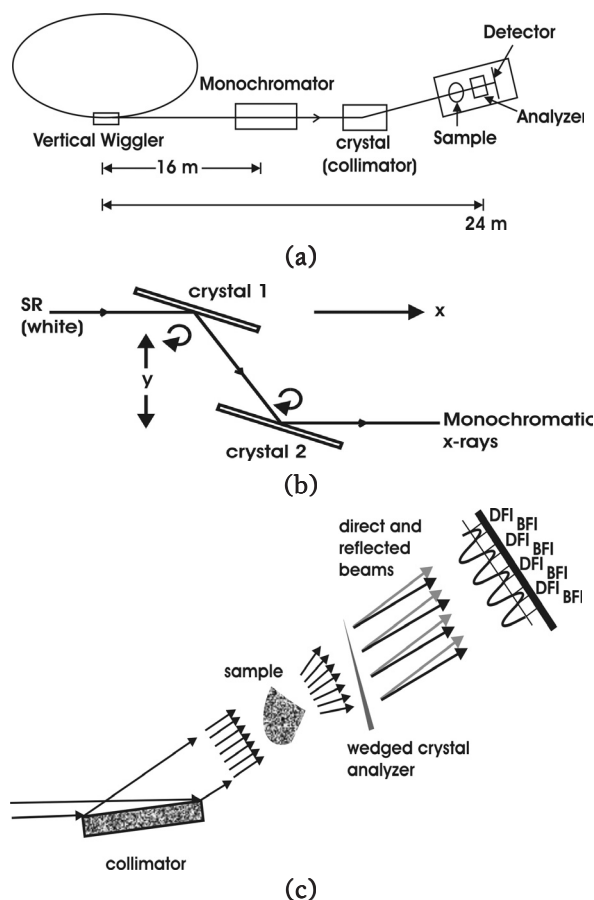


Fig 3. The conceptual illustration of the X-ray beam line (top panel), the principle of a double crystal analyzer (middle panel) and the layout of optical elements for the absorption image measurement (bottom panel).

both in the incident and diffracted beam directions out of the analyzer of a finite thickness. The exposure time for obtaining each picture was 1 to 2 min. Original synchrotron radiation was from a superconducting magnet wiggler with a magnetic field of 5 Tesla installed in the PF storage ring with an electron beam energy of 2.5 GeV. The beam duct of BL14 extracting synchrotron radiation from the wiggler is 2050 mm long. Its aperture at the synchrotron radiation outlet of the storage ring is 53 mm. The monochromator was slightly inclined upward. Under this condition, the dose rate on the sample is estimated at 0.0114 mSv/sec.

The specimen was the accreditation phantom RMI 156 comprising sixteen types of cancerous fibers, specks and discs which are embedded in wax. The phantoms were collected and fixed on an acrylic plate. When the image of each phantom was observed, each phantom was taken off from the acrylic plate and fixed on the sample holder. Thus, phantom x-ray pictures were taken without acrylic plate.

Just for the comparison of images, a plane parallel crystal analyzer was also used. In this case, the optical system was the same as that used for the wedged crystal analyzer. Only the crystal analyzer blade was replaced. In the case where a plane parallel analyzer is used, BFI and DFI are completely separated spatially and recorded on two different films. Experiments were carried out separately on BFI and DFI. Among various specimens prepared for this purpose, an ant was selected here to show a representative example.

EXPERIMENTAL RESULTS

The representative examples of DFI and BFI were compared in Fig. 4. Panels (a) and (b) show DFI and BFI of an ant, respectively. They were observed separately on different detector films using a plane parallel analyzer. In BFI shown in Fig. 4(b), the fringe part and the highly absorbing area of the specimen are resolved clearly. However, the interior of the body where the absorbance is not high, the features are not well visible.

In DFI shown in Fig. 4(b), the background disappears. This enhances the contrast and the structure of the interior of the body is better resolved. Since the data are taken on separate detector films by separate observations, the experimental condition and data processing are not the same in DFI and BFI observations. Thus, the data shown in Fig. 4(a) and (b) cannot provide a complete evidence of the validity of the assumption made on the angular profile of I_0 in depicting the angular profiles of BFI and DFI. The data shown in Fig. 4(a) and (b) cannot provide an evidence of the superiority of DFI to BFI, although the data appear to indicate the usefulness of DFI.

Fig. 4 (c) shows an example illustrating a better

contrast in DFI. The sample is a piece of the breast cancer phantom specimens RMI 156 No.2. The specimen contains a fiber simulating a cancer. The striped image pattern is shown. In this case, because of the short time for processing and printing of exposed film, the contrast of BFI is too low to illustrate the edge of the fiber in the specimen. As a result, the fiber image can be seen clearly only in DFI.

It is recognized that the dark band is narrower than the white band as expected from Fig. 2. If the important features of the sample fall on this area, however, we can see their better images can be seen in this region. The band shape is distorted in the part on the left-hand side of the figure. The width of the dark band is not uniform. Such distortion is brought about by the imperfect manufacturing of the crystal analyzer. The average relative intensities of dark field X-ray beams

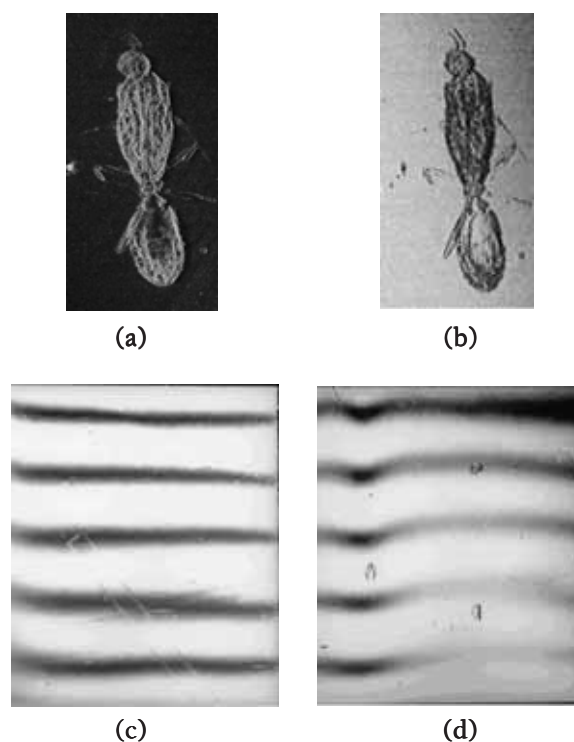


Fig 4. Dark-field image (a) and bright-field image (b) of an ant embedded in polymethylmethacrylate. A parallel plate crystal analyzer was used. The cross section of the X-ray beam incident on the sample is 5 mm x 5 mm. Exposure time was approximately 60 s. The dark-field image (a) has almost no background. Panels (c) and (d) show striped image patterns obtained by using a wedge-shaped analyzer. These examples show better contrast in dark field images. The cross section of the X-ray beam incident on the recorder film is 10 mm x 15 mm. Samples are the breast cancer phantom RMI 156; (c) specimen No. 2 and (d) specimen No. 6 (the specks simulate breast cancers.).

are about 25% as strong as those the bright field X-ray beams.

Fig. 4 (d) shows the recorded images of specks in the breast cancer phantom specimen RMI 156 No.6. Only the fringe parts of the specks are visible in BFI, while the inner structure of a speck is noticeable in DFI. The specks simulate cancers. Since DFI provides clear images of the cancer phantoms, it is recognized that DFI can be a useful means for the cancer diagnosis.

DISCUSSION

The present practical test experiments revealed a few problems to be solved in the future. They are summarized as follows:

- (i) The alignment of the optical system must be carried out very accurately.
- (ii) The crystal analyzer must be cut very accurately.
- (iii) Strong synchrotron radiation degrades the crystal analyzer.
- (iv) Chemical processing of exposed films (developing) and the printing of the image on a photographic paper affect the image contrast crucially.
- (v) The method to produce large DFI must be established.
- (vi) The record of the image must be made electronically. For instance, the use of a CCD camera should be considered. These facilitate the data processing by the use of a computer

A technique to reconstruct three dimensional images using the images that are of two dimensional in practice has been reported^{18, 19}. The technique is equivalent to CT scanning by the use of bright field imaging. The bright field absorption imaging has the limitation of the applications because various specimens, particularly those of excised human bodies, have low absorption contrast as the intrinsic nature. Thus, it is very much desirable to extend this technology to the dark field imaging.

A pioneering work to apply the image reconstruction technique of the two dimensional case to the dark field imaging has been carried out by Dilmanian²⁰ using a simple cancer phantom specimen. For realizing this, the optical system must be established so as to supply sufficiently good images with good contrasts. For establishing it, the photographic recording of images is only the initial stage of the investigation. This is implemented in present work. The present preliminary study has been successful. The samples of breast cancer phantom similar to ones used here were observed by Alfelli *et al.*²¹ and Fiedler *et al.*²². Our data give resolution and contrast better than those they obtained

When the major part of these basic techniques is achieved, the technique to record the image by

electronic methods as one with CCD cameras must be established. Then the computer software for the three dimensional reconstruction of the images is required.

As the future prospects of the work, we point out the importance of the expansion of images. In case of DFI, the principle of operation tells us that the expansion of the image is quite useful to separate BFI. This is particularly so in case of the optical system using the wedge-shaped crystal analyzer. In principle, this can be implemented by reducing the summit angle of the wedge appropriately.

In addition, to settle a very accurate optical system, the improvement in the data processing technique is also very important. This indirectly enhances the resolution and contrast of images. The use of the electronic recording is also indispensable. This is crucial for realizing X-ray microscopy in materials imaging.

ACKNOWLEDGEMENTS

The authors appreciate the Thailand Research Fund for the support and encouragement for the present study. W.P. would like to thank the Thailand Research Fund sincerely for the Royal Golden Jubilee Scholarship, which has enabled her to study at the Graduate University for Advanced Studies as an exchange PhD student.

REFERENCES

1. Hyodo K, Nishimura K and Ando M (1991) Coronary Angiography Project at Photon Factory Using a Large Monochromatic Beam. In: *Handbook on Synchrotron Radiation Vol. 4* (Edited by Ebashi S, Koch M and Rubenstein E), pp 55-94. North-Holland, Amsterdam Oxford New York Tokyo.
2. Ohtsuka S, Sugishita Y, Takeda T, Itai Y, Hyodo K and Ando M (1997) Dynamic intravenous coronary arteriography using synchrotron radiation and its application to the measurement of coronary blood flow. *Jpn. Circ. J.* **61-5**, 432-40.
3. Cosslet VE and Nixon WC (1953) The X-Ray Shadow Microscope. *J. Appl. Phys.* **24**, 616-23.
4. Bonse U and Hart M (1965) An x-ray interferometer. *Appl. Phys. Lett.* **6**, 155-6.
5. Ando M and Hosoya S (1972) An Attempt at X-ray phase contrast microscopy. In: *Proc. 6th Int. Conf on X-Ray Optics & Microanalysis* (Edited by Shinoda G, Kohra K and Ichinokawa T), pp. 63-68. Univ. of Tokyo, Tokyo.
6. Momose A, Takeda T, Itai Y, Yoneyama A and Hirano K (1998) Phase-contrast tomographic imaging using an X-ray interferometer. *J. Synchrotron Rad.* **5**, 309-14.
7. Ingal VN and Beliaevskaya EA (1995) X-ray plane-wave topography observation of the Phase contrast from a non-crystalline object. *J. Phys. D* **28**, 2314-7.
8. Wilkins SW, Gureyev TE, Gao D, Pogany A and Stevenson AW (1996) Phase-contrast imaging using polychromatic hard X-rays. *Nature* **384**, 335-8.
9. Clotens P, Barrett R, Guigay JR and Shlenker M (1996) Phase objects in synchrotron radiation hard X-ray imaging. *J. Phys. D* **29**, 133-46.
10. Chapman D *et al.* (1996) Mammography imaging studies using a Laue crystal analyzer. *Rev. Sci. Instr.* **67**, 3360.

11. Kittel C (1971) *Introduction to Solid State Physics*, Chapter 1, pp 1 – 42. John Wiley & Sons, Inc., New York, London, Sydney, and Toronto.
12. Krinsky S, Perlman M L and Watson R E (1983) Characteristics of Synchrotron Radiation and of its Sources. In: *Handbook on Synchrotron Radiation vol 1* (Edited by Koch E E), pp 67 – 171. North-Holland Publishing Co., Amsterdam, Oxford, New York and Tokyo.
13. Bowen, B K (1989) Principle of X-ray Diffraction Topography. In: *Applications of Synchrotron Radiation* (Edited by Winick H, Xian D, Ye M-H and Huang T), pp 77– 89. Gordon and Breach Science Publishers, New York, London, Paris, Montreux, Tokyo and Melbourne.
14. Pinsker ZG (1978) *Dynamical scattering of X-rays in crystals*. Springer-Verlag, New York.
15. Matsushita T and Hashizume H (1983) X-ray Monochromators. In: *Handbook on Synchrotron Radiation vol. 1* (Edited by Koch E E), pp 67 – 171. North-Holland Publishing Co., Amsterdam, Oxford, New York and Tokyo.
16. Batterman, B K (1989) Diffraction Principles Applied to Synchrotron Radiation. In *Applications of Synchrotron Radiation* (Edited by Winick H, Xian D, Ye M-H and Huang T), pp 77– 89. Gordon and Breach Science Publishers, New York, London, Paris, Montreux, Tokyo and Melbourne.
17. Thomlinson W, Chapman D, Zhong Z, Johnston R E and Sayers D (1998) Diffraction enhanced X-ray imaging. In: *Medical Applications of Synchrotron Radiation* (Edited by Ando M and Uyama C), pp. 72-7. Springer-Verlag, Tokyo.
18. DeFrise M, Clack R and Townsend D W (1995) Image reconstruction from truncated, two-dimensional, parallel projections. *Inverse Problems* **11**, 287-313.
19. DeFrise M, Townsend D W and Clack R (1989) Three-dimensional image reconstruction from complete projections. *Phys. Med. Biol.* **34(5)**, 573-87.
20. Dilmanian A (2000). Computed tomography of x-ray index of refraction using the diffraction enhanced imaging method. *Phys. Med. Biol.* **45**, 933-46.
21. Arfelli F *et al.* (2000) Mammography with synchrotron radiation: phase-detection techniques. *Radiology* **215**, 286-98.
22. Fiedler S, Bravin A, Thomlinson W, Keyrilainen J and Suortti P (2001) Prospects for Diffraction Enhanced Imaging Mammography. *Proc. of Joint Symposium on Bio-sensing and Bio-imaging* **1(B)-4**, 111.